

Full Spectroscopic Model and Trihybrid Experimental-Perturbative-Variational Line List for CN

Anna-Maree Syme¹, Laura K. McKemmish^{1*}

¹*School of Chemistry, University of New South Wales, 2052, Sydney, Australia*

May 31, 2021

ABSTRACT

Accurate line lists are important for the description of the spectroscopic nature of small molecules. While a line list for CN (an important molecule for chemistry and astrophysics) exists, no underlying energy spectroscopic model has been published, which is required to consider the sensitivity of transitions to a variation of the proton-to-electron mass ratio.

Here we have developed a DUO energy spectroscopic model as well as a novel hybrid style line list for CN and its isotopologues, combining energy levels that are derived experimentally (MARVEL), using the traditional/perturbative approach (MOLLIST), and the variational approach (from a DUO spectroscopic model using standard ExoMol methodology). The final Trihybrid ExoMol-style line list for ¹²C¹⁴N consists of 28,004 energy levels (6,864 experimental, 1,574 perturbative, the rest variational) and 2,285,103 transitions up to 60,000 cm⁻¹ between the three lowest electronic states (X ²Σ⁺, A ²Π, and B ²Σ⁺). The spectroscopic model created is used to evaluate CN as a molecular probe to constrain the variation of the proton-to-electron mass ratio; no overly promising sensitive transitions for extragalactic study were identified.

Key words: molecular data – techniques: spectroscopic

1 INTRODUCTION

CN is a molecule ubiquitous in astrochemistry that has been well studied experimentally and theoretically. CN shows initial promise as a potential molecular probe to constrain the variation of the proton-to-electron mass ratio (Syme et al. 2019; Syme & McKemmish 2020a), however an energy spectroscopic model of CN - not currently available - is required to identify key transitions of enhanced sensitivity.

The cyano (CN) radical was the second observed molecular species in the interstellar medium (McKellar 1940) and observed extra-galactically by Henkel et al. (1988). CN is one of the most widely distributed astrophysical molecules observed across the electromagnetic spectrum. For example, in the optical and visible, CN has been seen in interstellar clouds (McKellar 1940; Ritchey et al. 2011a), carbon stars (Barnbaum et al. 1996), and the Hale Bopp comet (Wagner & Schleicher 1997). In infrared, CN has been seen in comets (Huggins et al. 1881; Shinnaka et al. 2017), active galactic nuclei (Riffel et al. 2007), and sunspots (Harvey 1973). In the microwave region CN has been observed in the Orion nebula (Jefferts et al. 1970) and throughout diffuse clouds (Allen & Knapp 1978). CN provides insight into diverse astrophysical phenomena. CN stars (a peculiar type of carbon stars) have unusually strong CN peaks present in their spectra (Barnbaum et al. 1996). CN is often used as a tracer of

gas layers which are affected by photochemistry, and is predominantly found in regions exposed to ionizing stellar UV radiation (Riechers et al. 2007). The rotational temperature of CN is used to estimate the brightness of the cosmic microwave background (Ritchey et al. 2011b). CN is an important part of the HCN cycle, a key precursor in the synthesis of prebiotic molecules, such as nucleotides, amino acids, and lipid building blocks (Ferus et al. 2017),.

Modelling observations of astronomical or other gaseous environments accurately, and thus understanding these environments, requires high accuracy line lists - i.e. details of all the energy levels in a molecule and the strength of transitions between these levels. These in turn rely on high-quality experimental data. In the case of CN, we need to consider at least the three lowest lying electronic states, the X ²Σ⁺ ground state, the A ²Π state at 9243 cm⁻¹, and the B ²Σ⁺ state at 25752 cm⁻¹, as astrophysical observations of interactions between all of these electronic bands have been observed (Hamano et al. 2019). All available experimental data was recently compiled for ¹²C¹⁴N (Syme & McKemmish 2020b), which then used the MARVEL (Furtenbacher et al. 2007) procedure to extract empirical energy levels.

For CN, the most accurate available line list is the MOLLIST data (Brooke et al. 2014), which considers transitions between the three lowest electronic states of CN - i.e. the X ²Σ⁺, A ²Π and the B ²Σ⁺ states. Uses of the MOLLIST line list have included; constraining the chemical evolution of the local disc with C and N abundances (Botelho et al. 2020), modelling

* E-mail: l.mckemmish@unsw.edu.au

the impact of chemical hazes in exoplanetary atmospheres (Lavvas & Arfaux 2021), probing interstellar clouds (Welty et al. 2020), chemical abundance in stars that may harbour rocky planets from TESS data (Tautvaišienė et al. 2020), as well as observing the first A $^2\Pi$ -X $^2\Sigma^+$ (0,0) band in the interstellar medium Hamano et al. (2019).

The MOLLIST line list is computed using the so-called traditional model (or perturbative method), fitting experimental transition frequencies to a model Hamiltonian using PGopher (Western 2017) to obtain a set of spectroscopic constants which are then used to predict unobserved line frequencies along with *ab initio* dipole moments, see Brooke et al. (2014) for further details. The MOLLIST traditional model interpolates very accurately but does not extrapolate well because it is based on perturbation theory (Bernath 2020). The CN MOLLIST line list has no published underlying energy spectroscopy model (i.e. set of potential energy and coupling curves) suitable for testing the sensitivity of its molecular transitions to variation in the proton-to-electron mass ratio.

Variational line lists, such as those developed by ExoMol (Tennyson et al. 2020) and TheoReTS (Rey et al. 2016), are based on a spectroscopically fitted energy spectroscopic model - i.e. potential energy and coupling curves. One popular program to create a variational line list for diatomics is the nuclear motion program DUO which variationally solves the nuclear motion Schrodinger equation for coupled electronic states (Yurchenko et al. 2016; Tennyson & Yurchenko 2017). DUO has been successfully utilised to generate spectroscopic data for over 15 diatomic molecules (Tennyson et al. 2020).

These variational line lists "extrapolate more reliably because [they are] a more realistic and less empirical model" (Bernath 2020), but are not as accurate for each individual vibronic band due to the reduced number of free parameters and increased physical constraints. No variational line list and thus no energy spectroscopic model exists for CN prior to this paper. This missing spectroscopic model meant that CN could not be rigorously evaluated as a potential molecular probe for proton-to-electron mass variation in Syme et al. (2019).

Experimental accuracy for individual lines (often the strongest lines) can be achieved for traditional and variational line lists by replacing energy levels with experimentally-derived energy levels best obtained from a MARVEL inversion of all experimental transitions.

Both traditional and variational line lists have their advantages. To take best advantage of all diatomic spectroscopic data (reviewed by McKemmish (2021)), we propose here to use a novel trihybrid approach combining data from the traditional and variational approaches with the best available experimental data.

This paper is organised as follows. In Section 2, we describe the creation of the energy spectroscopic model and analyse the resulting variationally predicted energy levels in comparison to MOLLIST and MARVEL energy levels.

In Section 3, we add the intensity spectroscopic model and combine previous line list approaches to develop and explore a novel Trihybrid line list. Finally, in Section 4, we use the newly generate energy spectroscopic model from Section 2 to consider CN as a potential probe to constrain the variation of the proton-to-electron mass ratio, and calculate the sensitivity coefficient of transitions generated by the final spectroscopic model.

Table 1. Fitted parameters of potential energy curves for CN DUO spectroscopic model using extended Morse oscillator defined in Yurchenko et al. (2020). VE and AE are given in cm^{-1} , while the equilibrium bond lengths, RE, are given in \AA ; all other parameters are dimensionless. PL = 4, PR = 4, NL = 4 for all states while NR = 8, 5 and 10 for the X $^2\Sigma^+$, A $^2\Pi$ and B $^2\Sigma^+$ states respectively.

	X $^2\Sigma^+$	A $^2\Pi$	B $^2\Sigma^+$
VE	0.	9246.87	25755.6
RE	1.17272	1.23135	1.14979
AE	63619.4	63619.4	82843.1
B0	2.53904	2.40674	2.79379
B1	0.198393	0.122269	0.394873
B2	0.190872	0.155105	0.0593097
B3	0.241124	0.0809963	-1.81274
B4	0.369992	-0.110404	-1.94198
B5	-1.36549	0.701309	-3.24721
B6	2.54545		8.02791
B7	0.		0.
B8	-0.0865204		2.48582
B9			0.
B10			-5.03082

2 ENERGY SPECTROSCOPIC MODEL (ESM)

2.1 Construction

An energy spectroscopic model (ESM) consists of potential energy curves (PECs) for each electronic state and coupling curves between those states. ESMs for diatomic molecules can be constructed using DUO (Yurchenko et al. 2016; Tennyson & Yurchenko 2017), where each PEC and coupling curves are represented by a mathematical functions.

The parameters of these functions are fit using DUO to minimise the difference between the Duo-predicted variational energy levels and the available MARVEL experimentally-derived energy levels (Syme & McKemmish 2020b). DUO uses a grid-based sinc DVR method to solve the coupled Schrodinger equation; for our calculations, we use grid of uniformly distributed 1001 points from 0.6-4.0 \AA . This fit is highly non-linear and so fitting is normally done iteratively, often considering just one electronic or vibronic state at a time. The $v = 14, 16,$ and 18 states of the B $^2\Sigma^+$ state were unweighted in the DUO fit due to large perturbations. For further details of the fitting process, see Yurchenko et al. (2016); Tennyson & Yurchenko (2017); Tennyson et al. (2016). Of particular note for CN was the high vibrational and rotational quantum numbers for which experimental data is available; essentially removing the need for *ab initio* data as a starting point.

During the fitting process we identified a few misassignments in the MARVEL data. The transitions that these data was taken from were identified and removed; the updated MARVEL files are in the supplementary material.

Potential Energy Curves: The potential energy curves (PEC) for the X $^2\Sigma^+$, A $^2\Pi$, and B $^2\Sigma^+$ electronic states were described using the Extended Morse Oscillator (EMO) (Lee et al. 1999) with standard parameterisation, detailed in Section 2.1. The X $^2\Sigma^+$ and A $^2\Pi$ state have a common dissociation asymptote fixed to the experimental value of $63,619.4 \text{ cm}^{-1}$ (Huber & Herzberg 1979), whereas the B $^2\Sigma^+$ state has a higher dissociation limit fixed at $82,843.11 \text{ cm}^{-1}$ (Yin et al. 2018). To ensure a sufficient fit, a significant amount

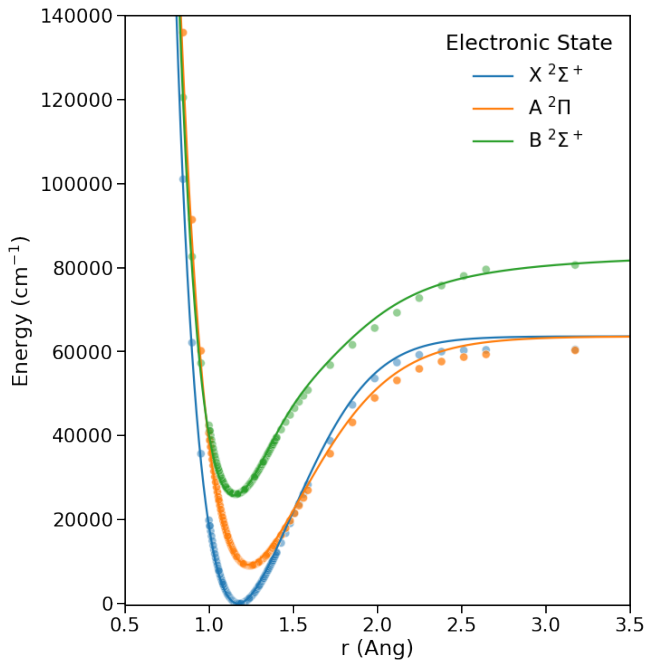


Figure 1. Potential energy curves of the 3 lowest electronic states of CN. The solid line shows the final curves fit using MARVEL energy levels, and the dots show the *ab initio* calculations.

of parameters were used to fit these states due to the large amount of experimental data including very high v and high J energy levels from MARVEL.

The resulting PECs are shown in Figure 1. Calculated *ab initio* curves are provided for reference but not used in the construction of the ESM due to the wealth of available experimental energy levels. The fitted and *ab initio* curves are very similar near the bottom of the potential well, with increasing deviation at larger r because the *ab initio* predicted dissociation energy differed from the experimental value. Our calculations used MRCI/aug-cc-pVTZ level with an (6,2,2,0) active space based on state-averaged ($X^2\Sigma^+$, $A^2\Pi$ and $B^2\Sigma^+$ only) Complete Active Space Self-Consistent Field (SA-CASSCF) calculations. We note that similar *ab initio* results are presented in, for example, Shi et al. (2011); Yin et al. (2018); however, underlying raw data could not be obtained, highlighting the importance of data accessibility (McKemmish 2021).

Coupling: The interaction of electronic states is described through a variety of coupling curves, all described using the Surkus-polynomial expansion (Yurchenko et al. 2016) to ensure correct asymptotic behaviour. Various diagonal and off-diagonal terms were included as part of the fit to the MARVEL energy levels, described in Table 2, with the most important term the diagonal spin-orbit coupling term for the $A^2\Pi$ state.

2.2 Analysis

Comparison of variational DUO with experimentally-derived MARVEL energy levels: Figure 2 visually compares the variational DUO energy levels to the experimentally-derived MARVEL energy levels as a function of energy. The mean, RMSD, and maximum absolute deviation

Table 2. Fitted constants, as defined in Yurchenko et al. (2016), affecting energy levels of individual electronic states: diagonal spin-spin (λ_{SS}), spin-rotational (γ_{SR}), rotational Born-Oppenheimer breakdown term (B_{rot}), spin-orbit (SO), and lambda doubling (λ_{p2q} , λ_{opq}) constants in cm^{-1} . Off-diagonal spin-orbit and electronic angular momentum coupling terms respectively

Diagonal	$X^2\Sigma^+$	$A^2\Pi$	$B^2\Sigma^+$
SO, B0		-26.5	
SO, B1		-7.22	
λ_{SS}	0.100	0.100	1.00
γ_{SR}	0.0131	-0.00370	0.0183
B_{rot}	0.00162	-0.00266	-0.00323
λ_{p2q}		0.0231	
λ_{opq}		-0.0277	
Off Diagonal	X, A	B, A	
SO	18.8	1.90	
L+	-0.368	-0.368	

for each vibronic level collated in Table 3. Overall, the $X^2\Sigma^+$ and $A^2\Pi$ states are very well fitted with an overall RMSD of 0.29 cm^{-1} and 0.21 cm^{-1} respectively. The $B^2\Sigma^+$ state is more problematic, but the rmsd is still 2.97 cm^{-1} , with errors dominated by the weaker fits in the strongly perturbed higher vibronic levels.

The first 2 panels for figure 2 show the deviation of the $X^2\Sigma^+$ state. We can see that the residuals of the $X^2\Sigma^+$ state are fairly consistent across each vibrational level, with the exception of $v = 17$ which has RMSD greater than 1 cm^{-1} . The maximum absolute deviation from the MARVEL energies in the $X^2\Sigma^+$ state is 3.01 cm^{-1} in the $v = 17$ state.

The $A^2\Pi$ state, shown in panels 3 and 4 show consistent errors for all vibronic states, with no vibronic level having an RMSD greater than 1 cm^{-1} , even the $v = 17$ state, which visibly looks scattered only has a rmsd of 0.67 cm^{-1} . The maximum deviation occurs in the $v = 17$ state, with an absolute deviation of 3.15 cm^{-1} . We see the diverging deviation in the lower vibronic levels of the $A^2\Pi$ state, while small, suggest an issue with the spin-spin coupling.

In the bottom two panels we see the deviation in the $B^2\Sigma^+$ state. While the $B^2\Sigma^+$ state is much higher in energy the deviation from the MARVEL energy levels seems especially large, and scattered. Over half of the vibronic levels in the $B^2\Sigma^+$ state have a RMSD greater than 1 cm^{-1} , and all but four vibronic levels have an RMSD greater than 0.5 cm^{-1} . The $v = 16$ to $v = 18$ have RMSD greater than 2.0 cm^{-1} . The maximum deviation of 37.95 cm^{-1} in the $B^2\Sigma^+$ state occurs at $J = 30.5$ and $v = 16$. The poor performance for high v levels in the $B^2\Sigma^+$ state is probably caused by perturbations that are not represented in our spectroscopic model, for example with the spectroscopically dark $4\Sigma^+$ state.

Comparison of variational and perturbative energy levels:

We compare the MOLLIST traditional/ perturbative energy levels with our variational energy levels by comparing the predicted energy levels against 6122 MARVEL empirical energy levels, visually in Figure 3 and quantitatively in Table 3. 86% of the energy levels MOLLIST are closer to the MARVEL empirical energy levels than those produced using the ESM in DUO. The improved behaviour arises because the

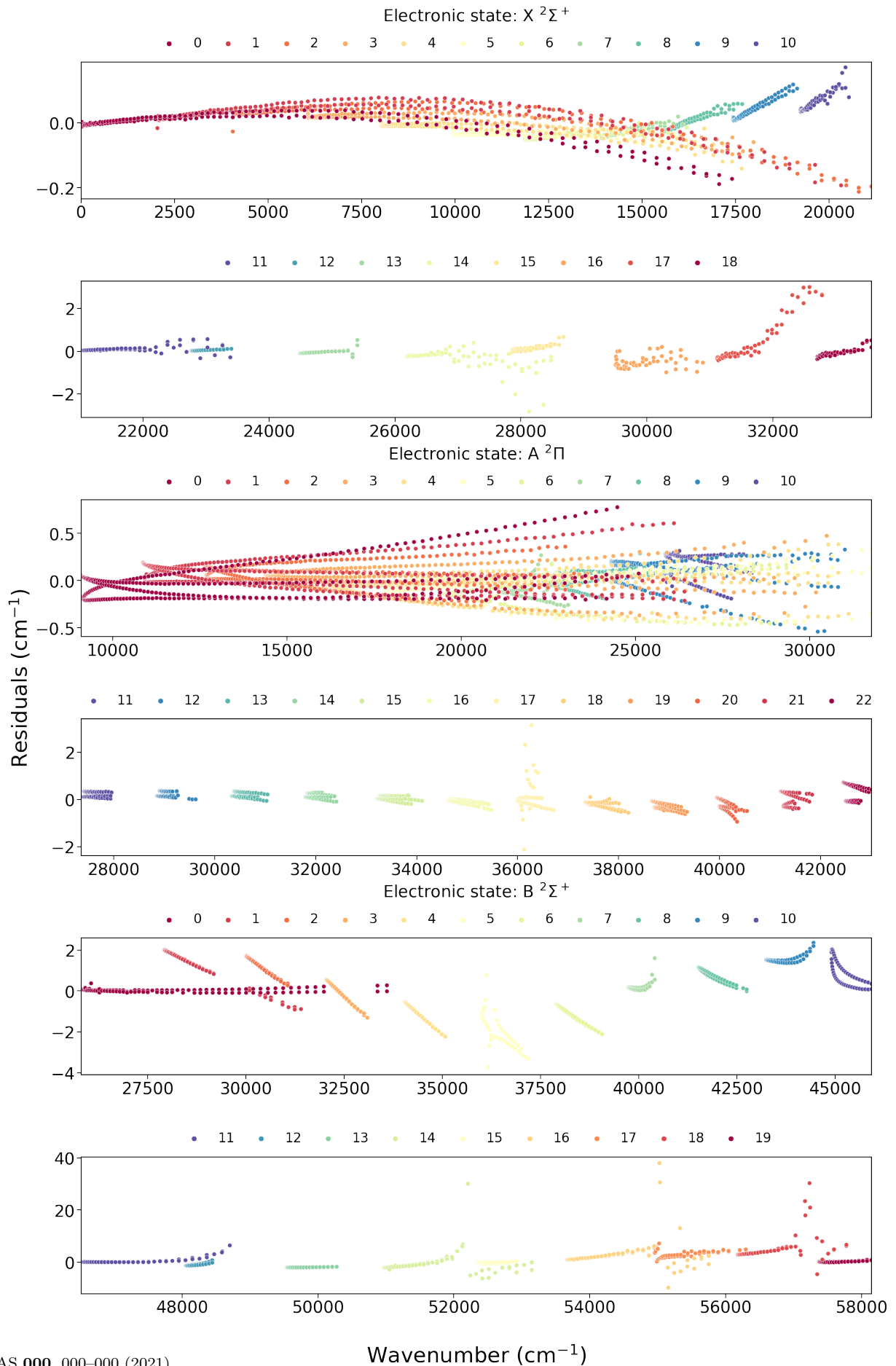


Table 3. Vibronic-scale breakdown of the average deviation of the DUO and MOLLIST energy levels from the MARVEL empirical energy levels. All deviations are in cm^{-1} .

v	Max J	DUO (this work) - MARVEL			MOLLIST - MARVEL		
		Mean	RMSD	Max	Mean	RMSD	Max
X $^2\Sigma^+$							
0	97.5	-0.01	0.05	0.19	-0.01	0.02	0.05
1	99.5	0.02	0.05	0.19	-0.01	0.02	0.05
2	97.5	0.01	0.06	0.21	-0.01	0.02	0.07
3	81.5	0.00	0.03	0.10	-0.01	0.02	0.03
4	72.5	-0.02	0.04	0.14	-0.01	0.02	0.05
5	60.5	-0.04	0.04	0.07	-0.01	0.01	0.03
6	48.5	-0.04	0.04	0.05	-0.00	0.01	0.05
7	36.5	-0.03	0.03	0.05	-0.01	0.01	0.03
8	34.5	0.01	0.03	0.06	-0.01	0.01	0.03
9	30.5	0.04	0.05	0.12	-0.01	0.01	0.02
10	27.5	0.07	0.07	0.17	-0.01	0.02	0.07
11	36.5	0.10	0.19	0.57	0.59	1.89	5.93
12	19.5	0.05	0.06	0.11	-0.00	0.02	0.05
13	23.5	-0.04	0.12	0.53	-0.00	0.10	0.52
14	37.5	-0.38	0.63	2.83	0.03	0.17	0.65
15	22.5	0.16	0.23	0.68	0.10	0.15	0.54
16	29.5	-0.51	0.58	0.99			
17	32.5	0.55	1.22	3.01			
18	23.5	-0.08	0.22	0.51			
A $^2\Pi$							
0	98.5	-0.02	0.20	0.78	-0.01	0.02	0.06
1	98.5	0.06	0.18	0.61	-0.01	0.01	0.03
2	80.5	0.07	0.14	0.36	-0.01	0.01	0.04
3	99.5	0.00	0.15	0.47	-0.02	0.11	1.14
4	97.5	-0.05	0.16	0.41	-0.00	0.08	0.98
5	94.5	-0.06	0.17	0.45	-0.04	0.30	3.14
6	82.5	-0.06	0.17	0.47	-0.08	0.41	3.83
7	37.5	-0.05	0.11	0.27	-0.30	1.15	4.82
8	41.5	0.02	0.09	0.29	0.27	1.05	7.61
9	65.5	0.06	0.19	0.54	-0.03	0.06	0.33
10	39.5	0.14	0.19	0.31	-0.01	0.03	0.28
11	19.5	0.21	0.24	0.35	-0.01	0.01	0.02
12	22.5	0.22	0.25	0.37	-0.00	0.01	0.03
13	21.5	0.20	0.23	0.36	-0.01	0.01	0.03
14	20.5	0.14	0.18	0.29	-0.01	0.01	0.02
15	23.5	0.05	0.11	0.19	-0.00	0.02	0.19
16	24.5	-0.08	0.13	0.44	-0.01	0.01	0.04
17	22.5	0.08	0.67	3.15	0.01	0.16	0.60
18	23.5	-0.22	0.25	0.56	-0.00	0.04	0.27
19	22.5	-0.30	0.33	0.62	-0.01	0.01	0.06
20	19.5	-0.26	0.34	0.94	-0.01	0.01	0.04
21	21.5	0.03	0.27	0.40	-0.01	0.02	0.13
22	20.5	0.30	0.45	0.72	-0.00	0.01	0.04
B $^2\Sigma^+$							
0	63.5	0.02	0.09	0.37	-0.01	0.03	0.16
1	41.5	1.15	1.46	2.01	-0.02	0.02	0.07
2	23.5	1.20	1.28	1.72	-0.02	0.03	0.07
3	23.5	-0.10	0.57	1.31	0.11	0.88	6.01
4	23.5	-1.16	1.27	2.23	-0.01	0.02	0.05
5	24.5	-1.91	2.09	3.72	0.02	0.37	1.71
6	25.5	-1.19	1.28	2.12	-0.01	0.01	0.02
7	19.5	0.22	0.35	1.60	-0.05	0.12	0.52
8	26.5	0.72	0.80	1.16	-0.01	0.01	0.04
9	26.5	1.55	1.56	2.35	-0.03	0.07	0.42
10	24.5	0.84	1.03	2.03	-0.00	0.09	0.33
11	36.5	0.51	1.23	6.43	-0.05	0.13	0.63
12	15.5	-0.89	1.01	1.28	-0.04	0.11	0.48
13	21.5	-2.00	2.00	2.12	-0.00	0.02	0.05
14	37.5	-0.74	4.35	30.08	-0.08	0.69	3.16
15	19.5	-0.20	0.31	0.62	0.08	0.13	0.50
16	37.5	2.66	6.45	37.95			
17	30.5	3.34	3.61	7.18			
18	33.5	5.20	7.30	30.28			
19	23.5	0.22	0.32	0.94			

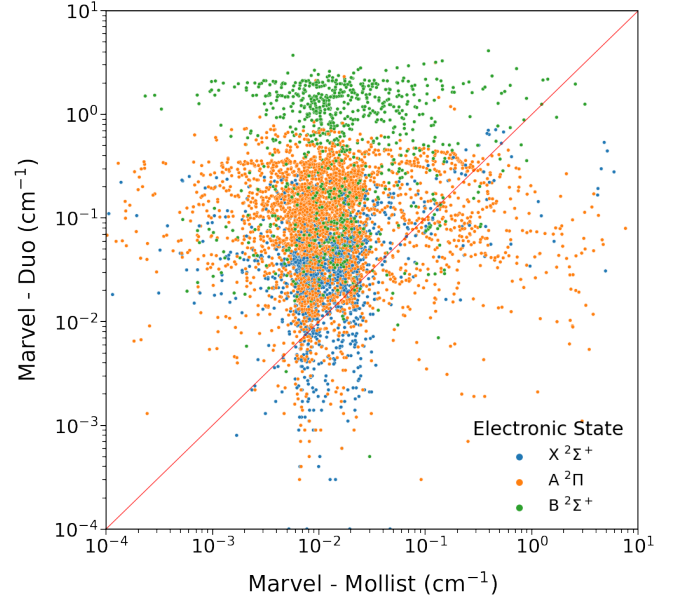


Figure 3. Comparison of the residuals with MARVEL empirical energy levels from MOLLIST and the DUO ESM.

MOLLIST perturbative method uses individual descriptions of each vibronic level enabling easier treatment of perturbations than a physically self-consistent ESM that must describe all vibronic levels. Table 3 does show some vibronic bands with significant MOLLIST errors, probably energies that were not included in the MOLLIST initial fit.

Spectroscopic constants: Table 4 compares the equilibrium spectroscopic parameters calculated by DUO for our fitted potential energy curves against existing data (Yin et al. 2018; Shi et al. 2011), including those used to construct MOLLIST. The parameters for the X $^2\Sigma^+$ state agree very well across all sources, with a small difference in ω_e and $\omega_e\chi_e$ in the computational values of Yin et al. (2018). The A $^2\Pi$ state has similar agreement across the sources, with a small difference of T_e values, but a much closer consensus on the ω_e and $\omega_e\chi_e$ values. The B $^2\Sigma^+$ state has the most disagreement across its equilibrium parameters. Our values for ω_e differ the most, and we see disagreement across all sources for $\omega_e\chi_e$. The difference between the Brooke et al. (2014) spectroscopic constants are our own are unlikely to be the primary reason for the differences in our predicted energy levels. Instead, the defining difference is likely to be the use of band constants in MOLLIST line list.

3 TRIHYBRID LINE LIST

A line list contains two files; a states (.states) file which lists all quantum states with their energies and quantum numbers and a transitions (.trans) file which details the strength of the transitions between states.

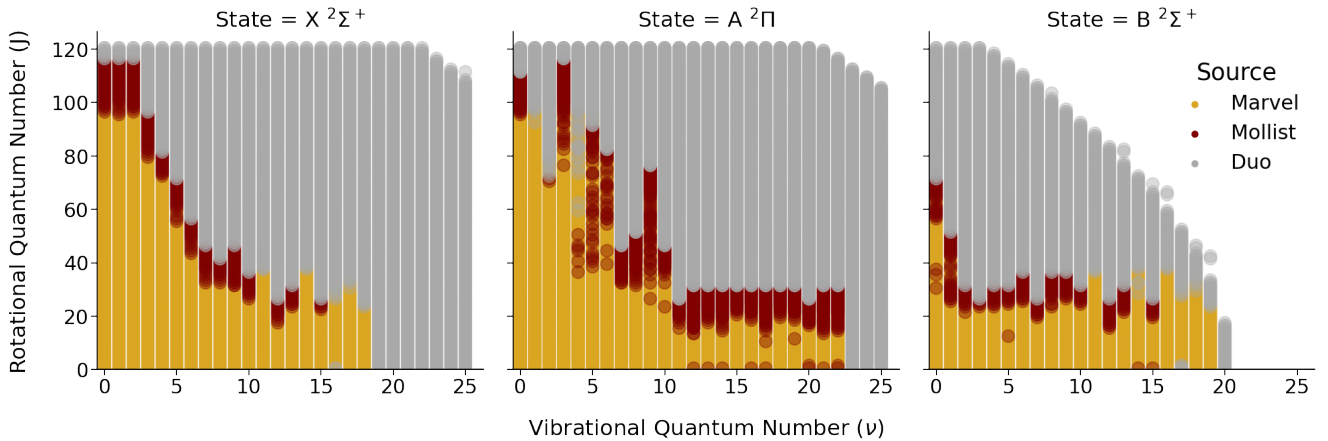
3.1 Energy Levels

Here we present a novel trihybrid approach for the construction of the final states file that combines energy levels from

Table 4. Spectroscopic equilibrium parameters for the 3 electronic states in the DUO spectroscopic model, compared with select values from the literature.

Electronic State	Parameter	This work	Brooke et al. (2014)*	Yin et al. (2018)	Huber & Herzberg (1979)	Babou et al. (2009)
X $^2\Sigma^+$	T_e	0.0000	0	0	0	0
	ω_e	2068.7230	2068.68325	2069.26	2068.59	2068.65
	$\omega_e\chi_e$	13.1808	13.12156	10.231	13.087	13.097
	B_0	1.8968	1.89978	1.9013	1.8997	1.899783
	R_e	1.1727	1.1718	1.1714	1.1718	-
A $^2\Pi$	α_e	0.0174	0.01738	0.01719	0.01736	0.01737
	T_e	9247.2180	9243.2959	9109.95	9245.28	9240
	ω_e	1812.8320	1813.288	1814.75	1812.56	1813.26
	$\omega_e\chi_e$	12.5944	12.77789	13.053	12.6	12.7687
	B_0	1.7205	1.7158	1.7174	1.7151	1.7159
B $^2\Sigma^+$	R_e	1.2314	1.233044	1.2324	1.2333	-
	α_e	0.0172	0.01725	0.01708	0.01708	0.017167
	T_e	25755.5900	25752.59	25776.42	25752	25752
	ω_e	2156.2630	2162.223	2163.04	2163.9	2161.46
	$\omega_e\chi_e$	16.2659	19.006	14.789	20.2	18.219
	B_0	1.9732	1.96797	1.9554	1.973	1.96891
	R_e	1.1498	1.15133	1.151	1.15	-
	α_e	0.0178	0.0188	0.01908	0.023	0.020377

* α_e for Brooke et al. (2014) was the opposite sign for all three states than other sources; we assume a definition difference.

**Figure 4.** Distribution of sources used to create the final states file broken down across electronic state, rotational quantum number (J), and vibrational quantum number (v), capped at $v = 25$ for brevity.

different sources to produce the most accurate and complete line list possible with current data and techniques.

The initial states file with 28,004 energy levels is produced with DUO using the variational approach with the ESM from Section 2. For each quantum state, the DUO energy is replaced when possible preferentially by MARVEL energies (6,864 levels) or otherwise by MOLLIST energies (1,574 levels) where available. For the three electronic states considered in this line list, we show the distribution of sources used in our final states file in Figure 4. Relatively few MOLLIST energies are included, probably due to the breadth of energy levels empirically determined in our MARVEL study (Syme & McKemmish 2020b).

Extracts of our final states files along with column descriptors, are shown in Table 5.

3.2 Intensity Spectroscopic Model

The intensity spectroscopic model consists of diagonal and off-diagonal (transition) dipole moments curves, calculated from high-level *ab initio* methods then extrapolated within DUO.

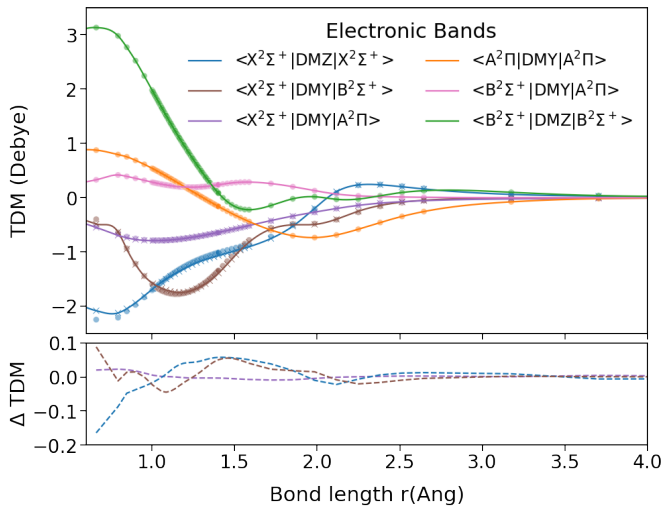
Using our state-averaged MRCI/aug-cc-pVTZ calculation methodology discussed above, we calculated all relevant dipole moment curves, shown as circles in Figure 5. This figure also shows the larger basis set results from Brooke et al. (2014) for the X $^2\Sigma^+$ -X $^2\Sigma^+$, A $^2\Pi$ -X $^2\Sigma^+$ and B $^2\Sigma^+$ -X $^2\Sigma^+$ curves as crosses. For our line list, we chose to use these larger basis set calculations for these curves, but note that there is only modest differences between the two *ab initio* methods (bottom subfigure); the modest impact of this choice on our final line list is discussed in the Supporting Information. We input our selected dipole moment data points as a grid into DUO, which fits a curve to these values.

We validate our *ab initio* results by comparing against experimental dipole moments. For the X $^2\Sigma^+$ and B $^2\Sigma^+$ states

Table 5. Extract from the state file for $^{12}\text{C}^{14}\text{N}$. Full tables are available at www.exomol.com and in the Supporting Information.

n	\tilde{E}	g_{tot}	J	unc	τ	g	+/-	e/f	State	v	Λ	Σ	Ω	Source	\tilde{E}_{DUO}
1	0.000000	6	0.5	0.001293	-1.00E+00	2.002305	+	e	X	0	0	0.5	0.5	M	0.000000
102	3.777245	6	0.5	0.003132	9.99E+04	-0.667444	-	f	X	0	0	-0.5	-0.5	M	3.775090
81	52340.028680	6	0.5	0.500000	1.27E-07	2.002272	+	e	B	15	0	0.5	0.5	P	52340.262410
132	28904.950010	6	0.5	0.500000	5.19E-06	-0.000931	-	f	A	12	-1	0.5	-0.5	P	28904.596730
78	51326.871830	6	0.5	1.000000	1.51E-05	-0.000658	+	e	A	30	1	-0.5	0.5	D	51326.871830
79	51797.529830	6	0.5	1.000000	9.39E-02	2.002186	+	e	X	32	0	0.5	0.5	D	51797.529830

Column	Notation	
1	n	Energy level reference number (row)
2	\tilde{E}	Term value (in cm^{-1})
3	g_{tot}	Total degeneracy
4	J	Rotational quantum number
5	unc	Uncertainty (in cm^{-1})
6	τ	Lifetime (s)
7	g	Landé factors
8	+/-	Total parity
9	e/f	Rotationless parity
10	State	Electronic state
11	v	State vibrational quantum number
12	Λ	Projection of the electronic angular momentum
13	Σ	Projection of the electronic spin
14	Ω	Projection of the total angular momentum ($\Omega = \Lambda + \Sigma$)
15	Source	Source of term value; M = MARVEL, P = MOLLIST (Brooke et al. 2014), D = DUO
16	\tilde{E}_{DUO}	Energy from DUO spectroscopic model


Figure 5. Dipole moment curves involving the three lowest electronic states of CN. The solid curves show the fitted DUO curves, the circles are *ab initio* calculations done in this work, and the crosses are the *ab initio* data from MOLLIST (Brooke et al. 2014)

respectively, the experimental values are 1.45 ± 0.08 D and 1.15 ± 0.08 D (Thomson & Dalby 1968), similar to our equilibrium dipole moment of 1.34 D and 1.17 D.

3.3 Transitions file

The final line list contains 2,285,103 transitions, covering the wavenumber range 0-60,000 cm^{-1} . The transitions file is produced by combining the rovibronic wavefunctions produced by the energy spectroscopy model with the intensity spectroscopic model. Transitions were calculated for states with

Table 6. Extract from the transition file for $^{12}\text{C}^{14}\text{N}$. Full tables are available from www.exomol.com and in the Supporting Information.

f	i	$A(f \leftarrow i) / \text{s}^{-1}$
181	1	0.000010
182	1	3.080700
183	1	0.216810
184	1	0.002965
185	1	0.004063

f : Upper (final) state counting number;
 i : Lower (initial) state counting number;
 $A(f \leftarrow i)$: Einstein A coefficient in s^{-1} .

lower energies up to 30,000 cm^{-1} as this contains 99 % of the total population at 5000 K. We have used a vibrational basis set up to $v = 120$ for each electronic state, and calculated rotational levels up to $J = 120.5$.

Extracts of our final transitions files along with column descriptors are shown in Table 6.

90% of strong transitions (defined as those with an intensity above $10^{-20} \text{cm}^2 \text{molecule}^{-1}$ at 1000 K) have wavenumbers fully computed from MARVEL energy levels; they are thus highly reliable and the line list is very suitable for use to detect molecules through high-resolution cross-correlation techniques in exoplanets. The remaining 10% of strong transitions contain one MARVEL energy level, with the other coming from the MOLLIST energy levels half of the time, and DUO predicted energy level the other half. Even considering all transitions with intensities over $10^{-33} \text{cm}^2/\text{molecule}$, fully MARVEL-ised transitions still make up 36% of the distribution, with only 13% of transition not containing any MARVEL energy level. Across all 2,285,103 transitions generated in the Trihybrid line list we see that 463,950 of them are fully MARVEL-ised, giving them pseudo-experimental accuracy. In

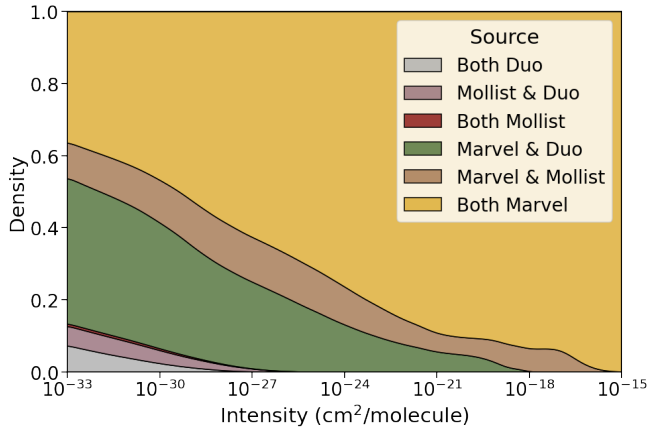


Figure 6. Cumulative density distribution of sources of energy levels in transitions across intensity, i.e. at each vertical slice, all transitions with intensities at or above the intensity at that x axis point are considered.

comparison the original MOLLIST line list includes 22,044 experimental transitions.

Figure 6 provides a more in-depth analysis by visually quantifying the source of the Trihybrid transition wavenumbers as a function of the cumulative transition intensity at 1000 K. Fully MARVEL-ised transitions dominate in all intensity windows above 10^{-25} $\text{cm}^2/\text{molecule}$.

3.4 Isotopologues

Full spectroscopic models and line list have been generated for three isotopologues of CN ($^{13}\text{C}^{14}\text{N}$, $^{12}\text{C}^{15}\text{N}$, and $^{13}\text{C}^{15}\text{N}$), and the states and trans file have been included in the supplementary information. The states files for these isotopologues have been pseudo-hybridised, as is standard for ExoMol isotopologue models (Polyansky et al. 2017), by shifting the energy levels of the isotopologues by the deviation between the main isotopologue DUO and MARVEL or MOLLIST energy, i.e. $E_{\text{new}}^{\text{iso}} = E_{\text{Duo}}^{\text{iso}} + (E_{\text{Trihybrid}}^{\text{main}} - E_{\text{Duo}}^{\text{main}})$ MOLLIST computed line lists for $^{13}\text{C}^{14}\text{N}$, $^{12}\text{C}^{15}\text{N}$ are also available from Sneden et al. (2014).

3.5 Results and Discussion

3.5.1 Partition function

The partition function for CN was calculated using ExoCross (Yurchenko et al. 2018) across 10-7000 K in steps of 10 K using the following equation:

$$Q(T) = \sum_n g_n^{\text{tot}} \exp^{-c_2 \bar{E}_n T}, \quad (1)$$

where g_n^{tot} is total degeneracy, $g_n^{\text{tot}} = g_n^{\text{ns}}(2J_n + 1)$, and g_n^{ns} is the ‘physics’ interpretation of the nuclear spin statistical weight factor (Pavlenko et al. 2020), $c_2 = hc/kB$ is the second radiation constant (cm K), $\bar{E}_i = E_i/hc$ are the energy term values (cm^{-1}), taken from the states file, and T is the temperature in K.

We compare our partition function to that of Sauval and Tatum (Sauval & Tatum 1984), Barklem and Collet (Barklem

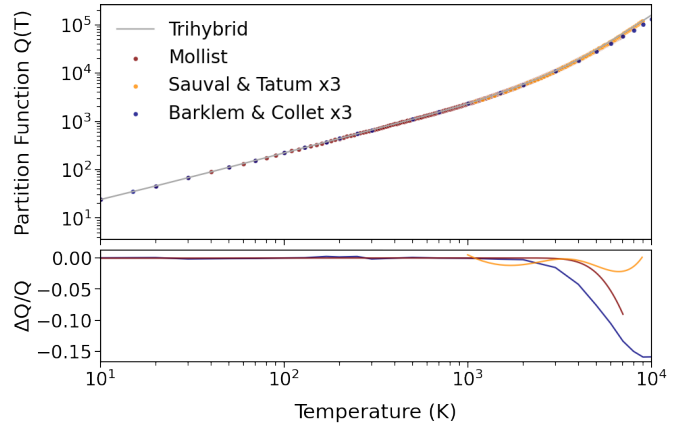


Figure 7. Comparison of the partition function for CN. Upper panel shows the partition function. Lower panel shows the relative deviation of each additional partition function to that from our hybrid states file. $(Q(\text{Other}) - Q(\text{Trihybrid})) / Q(\text{Trihybrid})$

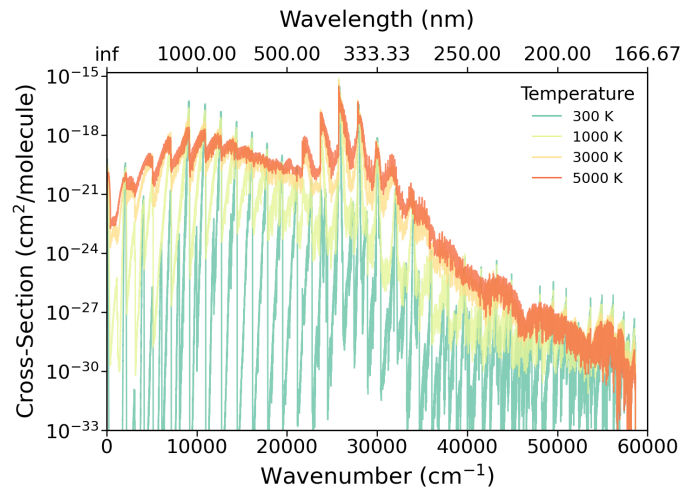


Figure 8. Cross section of CN up to $60,000 \text{ cm}^{-1}$ for temperatures between of 300, 1000, 3000, and 5000 K with HWHM at 2 cm^{-1} .

& Collet 2016), and the MOLLIST line list, as shown in figure 7. To make a direct comparison between our partition functions and those from Sauval & Tatum and Barklem & Collet we have multiplied their values by the nuclear spin statistical weight for CN; $g_n^{\text{ns}} = 3$ to be in the ‘physics’ convention which is used by ExoMol. All four partition functions show a strong agreement with a maximum relative deviation from the Trihybrid partition function of 0.16 from Barklem & Collet at 10,000 K.

3.5.2 Cross sections

Overview We computed the absorption cross-section at temperatures of 300 K, 1000 K, 3000 K, and 5000 K, using a gaussian line profile with a half width half maximum (HWHM) of 2 cm^{-1} in ExoCross, shown in figure 8. The spectra gets less defined with the increase in temperature, as expected. Above $35,000 \text{ cm}^{-1}$ we see a very broadened cross section, losing almost all form at higher temperatures.

Decomposing the absorption cross section at 1000 K into

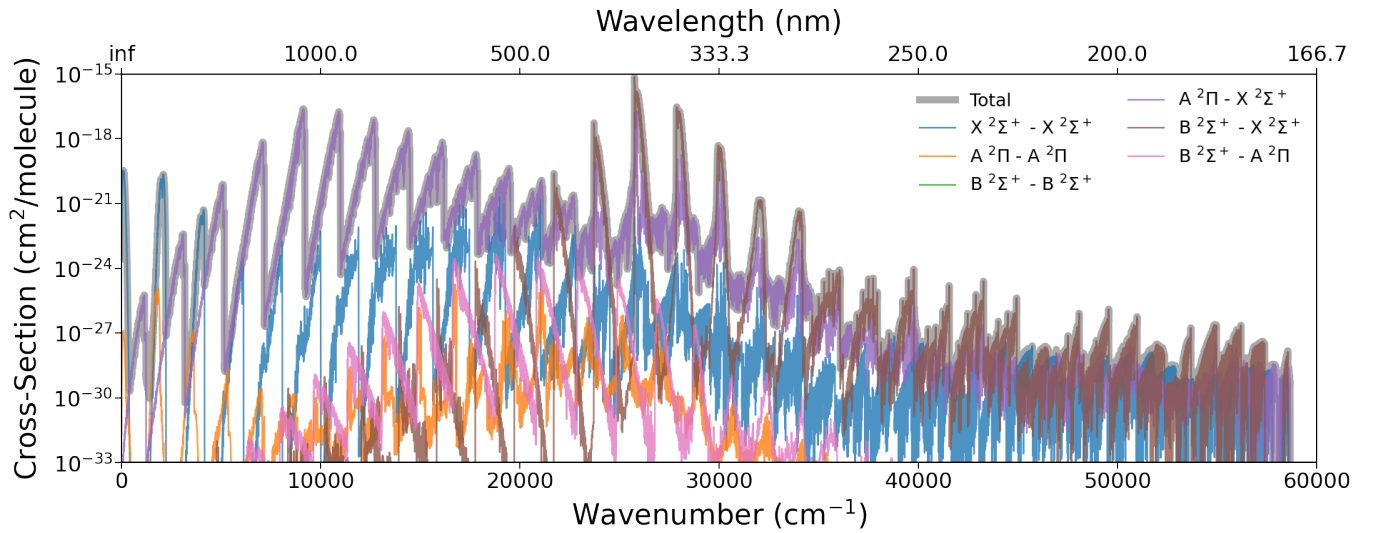


Figure 9. Cross section of CN from 0 - 60,000 cm^{-1} at 1000 K with HWHM at 2 cm^{-1} , divided into component electronic bands.

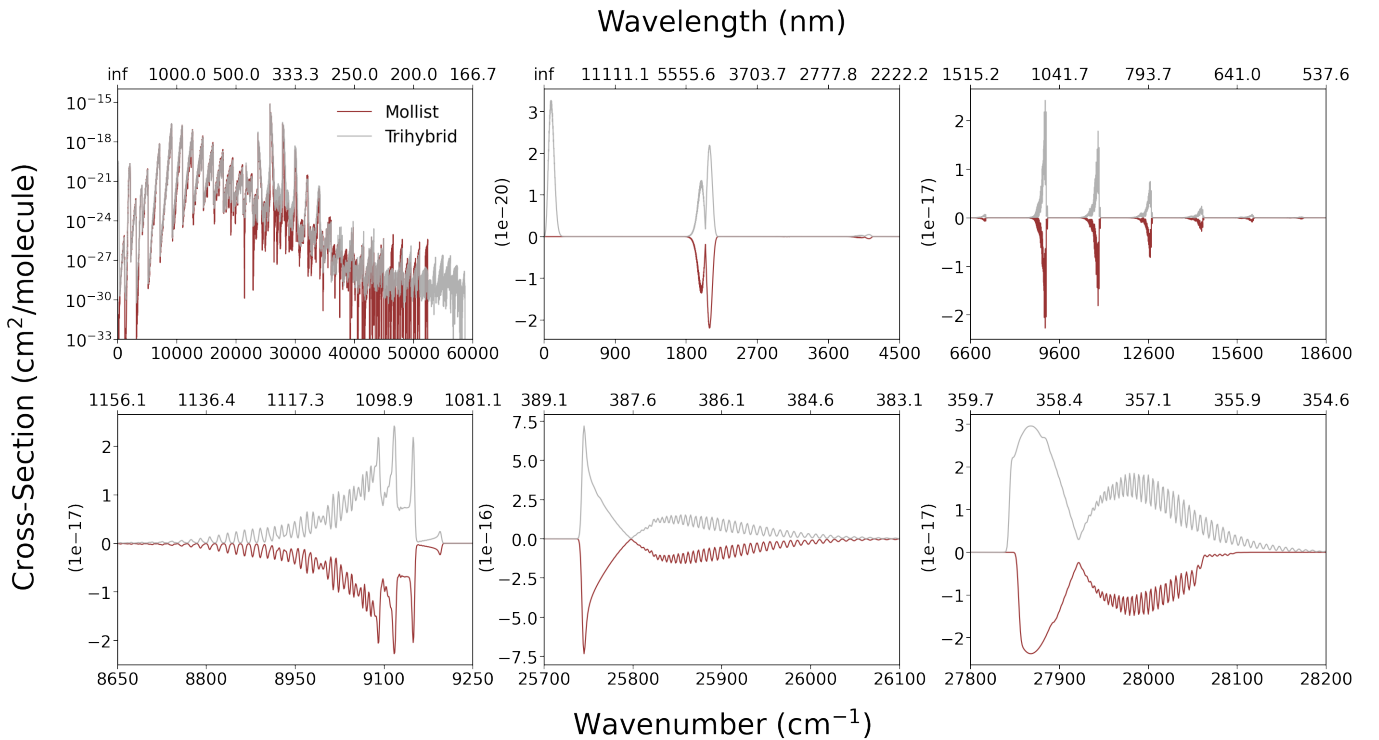


Figure 10. Comparison of the MARVELised MOLLISTline list cross section compared to the hybrid DUO line list at 1000 K, at different wavenumber ranges.

the bands in figure 9 we see a strong dominance across all wavenumbers from the $A^2\Pi-X^2\Sigma^+$ band. The $X^2\Sigma^+-X^2\Sigma^+$ band sees a strong occurrence in the microwave region before dropping off significantly, while the $B^2\Sigma^+-X^2\Sigma^+$ bands is very diminished at lower frequencies, but taking dominance above 25,000 cm^{-1} . The strongest feature of the spectra has a cross sectional intensity up to $10^{-15} \text{ cm}^2 \text{ molecule}^{-1}$ in the visible region, however there are strong ($< 10^{-20} \text{ cm}^2 \text{ molecule}^{-1}$) peaks within the infrared, microwave, and ultra-violet regions as well.

Comparison with the MOLLIST line list In the first sub-figure of figure 10 we compare the full cross section of the MOLLIST line list and our hybrid line list from 0 - 60, 000 cm^{-1} modelled at 1000 K with a HWHM of 2 cm^{-1} using ExoCross. We see the completeness that is gained from the DUO addition to the hybrid line list. The MOLLIST line list has a similar cross section, especially at lower wavenumbers, however decomposes with an increase in wavenumber. We can see the MOLLIST line list doesn't extend much further than 50,000 cm^{-1} , whereas the Trihybrid data extends much more smoothly out to 60,000 cm^{-1} . The other panels of fig-

ure 10 compare the MOLLIST cross sections and Trihybrid line list at a selection of key features. At wavenumber less than 4500 cm^{-1} we can see that the MOLLIST line list does not contribute at all to the low frequency rotation lines, and while the Trihybrid does not include hyperfine transitions, it does still consider these rotational lines. The main infrared band is clearly matched well around 2000 cm^{-1} . The A $^2\Pi$ -X $^2\Sigma^+$ bands shown between 6600 and 18600 cm^{-1} are also well matched. This is highlighted when we consider the main A $^2\Pi$ -X $^2\Sigma^+$ (0,0) band around 9000 cm^{-1} , with peak positions and intensities matching extremely well. We begin to see some more obvious discrepancies between MOLLIST and Trihybrid at higher energy. The main feature of the spectra (the B $^2\Sigma^+$ - X $^2\Sigma^+$ band) is matched pretty well at 25750 cm^{-1} but deviates above 27800 cm^{-1} due to the lower number of rotational energy levels included in the MOLLIST line list. Additional comparisons are provided in the Supporting Information.

3.5.3 Rotational Spectroscopy

Our new trihybrid model contains the rotational transition data for all lower states with energies less than $30,000\text{ cm}^{-1}$, thus comprehensively incorporating all rotational hot bands; recall that the MoLLIST data had no rotational transitions. However, for applications within microwave astronomy that focus on detecting a small number of strong lines, the existing CDMS data (collation (Müller et al. 2001, 2005) sourced from Dixon & Woods (1977); Skatrud et al. (1983); Johnson et al. (1984); Klisch et al. (1995)) is likely preferable due to the incorporation of hyperfine splitting that cannot yet be included in a DUO spectroscopic model (though future updates plan to add this feature to the program). CDMS has data for rotational transitions originating in the $v = 0$ and $v = 1$ states and can thus predict the strongest intensity hot bands.

Averaging over hyperfine structure, our line positions and the CDMS values agree well with a RMSD of 0.002 cm^{-1} , while the agreement in the Einstein A coefficients is good with a RMSD of 0.012 s^{-1} , reflecting the close agreement between the experimental dipole moment used by CDMS and the equilibrium value of the X $^2\Sigma^+$ state diagonal dipole moment curve used in our calculations.

3.5.4 Lifetimes

As discussed in McKemmish (2021), comparison of theoretical and experimental state lifetimes provide one of the most practical ways to validate the quality of *ab initio* off-diagonal transition dipole moment curves and thus the predicted intensities for rovibronic transitions. Therefore, in Table 7, we compare our calculated excited state lifetimes with existing experimental and theoretical values.

The B $^2\Sigma^+$ state results in Table 7 are straightforward; our results are within experimental uncertainties with strong agreement with MOLLIST (i.e. Brooke et al. (2014)) and reasonable agreement with other theoretical results.

The A $^2\Pi$ state results, however, are more concerning. Our results are in close agreement with MOLLIST and in reasonable agreement with other theoretical results. However, the two experimental results differ considerably (sometimes more

than a factor of 2) from both each other and from all *ab initio*-derived results. New experimental measurements would be highly desirable to validate or dispute the theoretical lifetimes (and thus the underlying dipole moment curves and predicted transition intensities). Astronomical or laboratory comparisons of the relative transition intensities in the A $^2\Pi$ -X $^2\Sigma^+$ and B $^2\Sigma^+$ -X $^2\Sigma^+$ bands (perhaps near the $20,000\text{ cm}^{-1}$ region where both bands have comparable intensity) could also provide evidence to resolve this theory-experimental discrepancy.

4 PROBE TO CONSTRAIN THE VARIATION OF THE PROTON-TO-ELECTRON MASS RATIO

CN was identified as a potentially promising molecular probe to constrain the variation of the proton-to-electron mass ratio in Syme et al. (2019). This paper found that diatomic molecules with low lying electronic states show a sizeable amount of enhanced sensitive transitions to a variation of the proton-to-electron mass ratio. CN was further isolated as a potential probe due to its abundance and chemical properties. CN is one of very few molecules that has been detected at high redshift ($z = 2.56$ and 3.9) (Riechers et al. 2007; Guélin et al. 2007) along with H_2 , HCN, CO, HCO^+ . The presence of CN at high red shift is significant when probing large time separation for constraining fundamental constants, such as the proton-to-electron mass ratio. A key driver of the construction of the spectroscopic model created in this work was to test the transitions of CN for their sensitivity and evaluate the efficacy of CN as a molecular probe.

4.1 Methodology

In Syme et al. (2019); Syme & McKemmish (2020a), we simulated a variation in the proton-to-electron mass ratio in diatomic molecules using spectroscopic models. We calculated the sensitivity of the transitions, K , in these diatomic molecules by matching the transitions on their id number in each simulation and using equation 2 with the matched transition frequencies using

$$\frac{\Delta\nu}{\nu} = K \frac{\Delta\mu}{\mu}, \quad (2)$$

where $\frac{\Delta\nu}{\nu} = \frac{\nu_{\text{shifted}} - \nu}{\nu}$ is the relative change in the transition frequencies, K is the sensitivity coefficient, and $\frac{\Delta\mu}{\mu}$ is the fractional change in the proton-to-electron mass ratio, simulated by a shift in the molecular mass.

As mentioned in the paper, there was a possibility that the id for the transitions was changed in the simulations and possible errors and miscalculations could arise. This method has been refined by matching the QNs of the energy levels from the states files and not using the transition id to identify a match. By matching on the QNs of the energy level we can account for the ordering of the states to change by the shift in the molecular mass. We have thus amended our approach to instead use

$$K_{\mu}(i \rightarrow j) = \frac{E_j k_j - E_i k_i}{E_j - E_i}, \quad (3)$$

where E is the energy of the lower (E_i) and upper (E_j) energy

Table 7. Comparison for lifetimes (ns) for vibrational states of the A $^2\Pi$ and B $^2\Sigma^+$ electronic states.

v	Line List		Experimental			Theory	
	This Work	MOLLIST	Lu et al. (1992)	Duric et al. (1978)	Yin et al. (2018)	Lavendy et al. (1984)	
A $^2\Pi$							
0	10735	11185	-	-	9980	11300	
1	9457	9680	-	-	9900	9600	
2	8515	8595	6960 \pm 300	3830 \pm 500	9670	8400	
3	7797	7785	5090 \pm 200	4050 \pm 400	8760	7600	
4	7234	7165	3830 \pm 200	3980 \pm 400	8040	6900	
5	6784	-	3380 \pm 200	4200 \pm 400	7400	6400	
6	6419	-	2260 \pm 200	4350 \pm 400	6960	6000	
7	6131	-	1840 \pm 300	4350 \pm 400	6540	5700	
8	6054	-	-	4500 \pm 400	6190	5400	
9	5659	-	-	4280 \pm 400	5890	5200	
10	5472	-	-	4100 \pm 400	5640	-	
11	5318	-	-	-	5430	-	
12	5188	-	-	-	5270	-	
13	5077	-	-	-	5120	-	
B $^2\Sigma^+$							
0	62.77	62.74	-	63.8 \pm 0.6	61.37	72	
1	62.88	62.97	-	66.3 \pm 0.8	55.53	72	
2	63.22	63.46	-	64.4 \pm 2.0	58.14	73	
3	63.82	64.25	-	65.6 \pm 3.0	59.74	75	
4	64.75	65.39	-	68.1 \pm 4.0	59.6	76	
5	66.08	66.95	-	67.3 \pm 5.0	60.79	78	
6	67.90	-	-	-	62.95	80	
7	70.28	-	-	-	64.45	82	
8	73.31	-	-	-	67.05	85	
9	77.04	-	-	-	70.41	88	
10	81.60	-	-	-	74.79	-	
11	86.75	-	-	-	80.11	-	
12	92.71	-	-	-	87.68	-	
13	99.70	-	-	-	91.68	-	

levels of the transitions, and k is the sensitivity coefficients of the lower (k_i) and upper (k_j) energy levels in a transition.

In the refinement of our method for calculating the sensitivity of transitions in diatomic molecules we found significant changes to the maximum sensitivity in some of the diatomic molecules investigated. While the conclusions we drew from our results in [Syme et al. \(2019\)](#) remain the same, individual molecules have new results. The most dramatic change in the results for a single molecule was SiH, with a change in maximum ΔK from ≈ 9 to ≈ 900 .

We continue to use the terminology of ‘enhanced’ transitions to describe transitions with a sensitivity coefficient $|K| > 5$. Again we only consider transitions below the intensity cutoff of $I < 10^{-30}$ cm² molecule⁻¹ at 1000 K.

4.2 Results for CN

Similar to the results in [Syme et al. \(2019\)](#) we see, in figure 11, that the enhanced transitions of CN have low transition frequencies (< 1000 cm⁻¹) and involve the ground electronic state, X $^2\Sigma^+$ and the first excited electronic state, A $^2\Pi$. We note here that while there are 731 enhanced transitions in CN, all have intensities below 10^{-26} cm² molecule⁻¹ at 1000 K, and the lowest energy level of the enhanced transitions is greater than 9000 cm⁻¹. These limiting factors suggest that the enhanced transitions in CN might not be observable in

the astrophysical environments that are probed to test the variation of the proton-to-electron mass ratio.

Given the observation of CN extra-galactically, it is worth considering whether stronger transitions with more modest K could be useful. Restricting our search to intensities greater than 10^{-20} cm² molecule⁻¹ at 1000 K, we find that UV/optical transitions with K values from -0.53 to 0.30 are observed, an order of magnitude larger than sensitivities obtained with H₂ transitions. However, UV/optical transitions are yet to be observed extragalactically for CN. Rotational transitions that have been observed extragalactically all have the sensitivity of pure rotational transitions, i.e. -1, not useful for a search for proton-to-electron mass variation.

4.3 Other diatomic molecules

A key finding in [Syme et al. \(2019\)](#) was the relationship between the energy of the first allowed excited state and the maximum sensitivity possible of the transitions considered. Here we provide an update on this relationship, shown in figure 12 which has the addition of CN and the sensitivities calculated from the recently published spectroscopic model for CP ([Qin et al. 2021](#)). We can see that while some of the data in this figure is different to that of figure 7 of [Syme et al. \(2019\)](#) the relationship remains consistent.

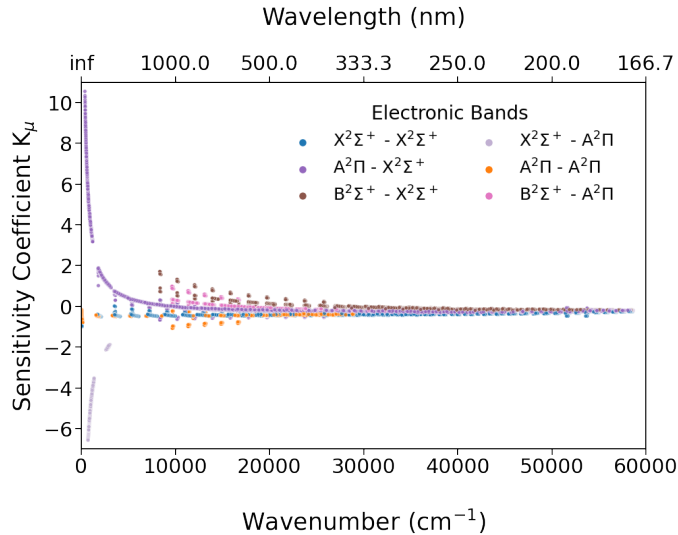


Figure 11. Spread of sensitivity of transitions within CN across energy.

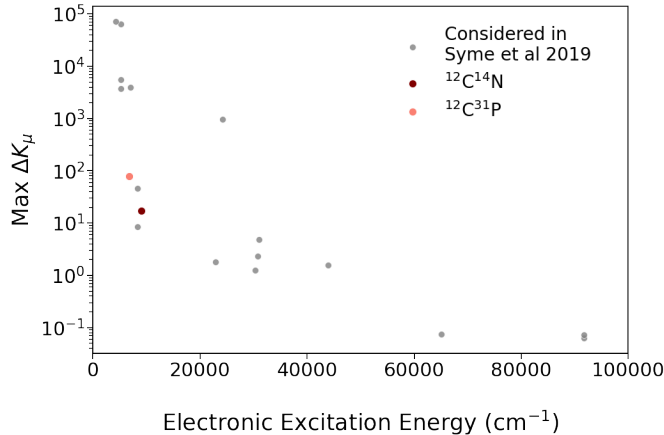


Figure 12. Relation between the energy difference of the ground electronic state and the first spin/symmetry allowed excited electronic state and the maximum $|\Delta K|$ with the new inclusions of CP, and CN.

4.4 Future directions

The refined method of calculating the sensitivity coefficients of transitions within molecules with the energy levels will allow us to scale up to larger molecules with reasonable computational cost. We look forward to taking advantage of this with future work into the sensitivity to a variation of the proton-to-electron mass ratio of transitions within polyatomic molecules.

5 CONCLUSIONS

The complete Trihybrid line list for CN can be found online at www.exomol.com and in the Supplementary Information in the ExoMol format. The line list contains 2,285,103 transitions between 28,004 energy levels from the 3 lowest electronic states ($X^2\Sigma^+$, $A^2\Pi$, and $B^2\Sigma^+$) of the main isotopologue of CN. The final states file combines energy levels

from MARVEL, MOLLIST, and ExoMol methodologies to produce a highly accurate and highly complete line list suitable for the full range of astrophysical applications from molecule detection using high-resolution cross-correlation techniques to modelling atmospheres to high precision.

Of particular note is our method of constructing the states file that combines experimentally derived empirical energy levels, energy levels from model hamiltonians and from variationally determined energy levels to produce the most accurate states file. This is a good approach moving forward and we expect to see many future line lists utilising this approach of line list generation.

A key motivator of this work was the development of a spectroscopic model to evaluate the efficacy of CN as a molecular probe to constrain the variation of the proton-to-electron mass ratio. While the sensitivities of the transitions within CN are not particularly enhanced, we do see some potential for CN to be used as a molecular probe if UV/optical transitions can be detected as it is a common molecule in various astrophysical environments.

ACKNOWLEDGEMENTS

We would like to thank Juan C. Zapata Trujillo for insightful comments on the manuscript.

This research was undertaken with the assistance of resources from the National Computational Infrastructure (NCI Australia), an NCRIS enabled capability supported by the Australian Government.

The authors declare no conflicts of interest.

DATA AVAILABILITY STATEMENT

The data underlying this article are available in the article and in its online supplementary material. These include the following files;

- DUO spectroscopic model and input file (12C-14N__Trihybrid_Duomodel.inp)
- Trihybrid states file (12C-14N__Trihybrid.states);
- Trihybrid transitions file for $^{12}\text{C}^{14}\text{N}$ (12C-14N__Trihybrid.trans);
- Partition function up to 10,000 K for $^{12}\text{C}^{14}\text{N}$ (12C-14N__Trihybrid.pf);
- Isotopologue states and transition files (in the isotopologue folder);
- A sample ab initio input file (multi_ci_SO_1.35.inp);
- csv file containing the PEC, TDM, and SOC from all of the *ab initio* calculations (abinitio_results.csv);
- Updated MARVEL transitions and energy levels (12C-14N_MARVEL_2021update.txt and 12C-14N_MARVEL_2021update.energies respectively).

We note that the data generated in section 4 can be reproduced through the use of the CN spectroscopic model given here, as well as the available spectroscopic models on the ExoMol website (www.exomol.com), using the method described in the paper.

ADDITIONAL SUPPORTING INFORMATION

As well as the data files described above, we include as supporting information two additional figures and associated discussion comparing (a) the new trihybrid and existing MOLLIST line lists and (b) the new trihybrid line list created using the MOLLIST X-X, A-X and B-X dipole moment curves compared to the the results when using our new smaller set result curves.

For clarity, all supporting information files are described in README_SI_CN_linelist.pdf.

References

- Allen M., Knapp G. R., 1978, *The Astrophysical Journal*, 225, 843
- Babou Y., Rivière P., Perrin M.-Y., Soufiani A., 2009, *Int J Thermophys*, 30, 416
- Barklem P. S., Collet R., 2016, *Astronomy and Astrophysics*, 588, 96
- Barnbaum C., Stone R. P. S., Keenan P. C., 1996, *The Astrophysical Journal Supplement Series*, 105, 419
- Bernath P. F., 2020, *Journal of Quantitative Spectroscopy and Radiative Transfer*, 240, 106687
- Botelho R. B., De Milone A. C., Meléndez J., Alves-Brito A., Spina L., Bean J. L., 2020, *Monthly Notices of the Royal Astronomical Society*, 499, 2196
- Brooke J. S. A., Ram R. S., Western C. M., Li G., Schwenke D. W., Bernath P. F., 2014, *The Astrophysical Journal Supplement Series*, 210, 23
- Dixon T. A., Woods R. C., 1977, *The Journal of Chemical Physics*, 67, 3956
- Duric N., Erman P., Larsson M., 1978, *Physica Scripta*, 18, 39
- Ferus M., Kubelík P., Knížek A., Pastorek A., Sutherland J., Civiš S., 2017, *Nature Scientific Reports*, 7, 6275
- Furtenbacher T., Császár A. G., Tennyson J., 2007, *Journal of Molecular Spectroscopy*, 245, 115
- Guélin M., et al., 2007, *Astronomy & Astrophysics*, 16, 45
- Hamano S., et al., 2019, *The Astrophysical Journal*, 881, 143
- Harvey J. W., 1973, *SOLAR PHYSICS*, 28, 43
- Henkel C., Mauersberger R., Schilke P., 1988, *Astronomy & Astrophysics*, 201, 23
- Huber K. P., Herzberg G., 1979, in *Molecular Spectra and Molecular Structure*. Van Nostrand Reinhold Company, New York, p. 498, doi:10.1007/978-1-4757-0961-2
- Huggins W., Huggins William 1881, *RSPS*, 33, 1
- Jefferts K. B., Penzias A. A., Wilson R. W., 1970, *The Astrophysical Journal*, 161, L87
- Johnson M., Alexander M., Hertel I., Lineberger W., 1984, *Chemical physics letters*, 105, 374
- Klisch E., Klaus T., Belov S., Winniewisser G., Herbst E., 1995, *Astronomy and Astrophysics*, 304, L5
- Lavendy H., Gandara G., Robbe J. M., 1984, *Journal of Molecular Spectroscopy*, 106, 395
- Lavvas P., Arfaux A., 2021, *Monthly Notices of the Royal Astronomical Society*, 502, 5643
- Lee E. G., Seto J. Y., Hirao T., Bernath P. F., Le Roy R. J., 1999, *Journal of Molecular Spectroscopy*, 194, 197
- Lu R., Huang Y., Halpern J. B., 1992, *The Astrophysical Journal*, 395, 710
- McKellar A., 1940, *The Astronomical Society of the Pacific*, 52, 187
- McKemmish L. K., 2021, *WIREs Computational Molecular Science*, p. e1520
- Müller H. S., Thorwirth S., Roth D., Winniewisser G., 2001, *Astronomy & Astrophysics*, 370, L49
- Müller H. S., Schlöder F., Stutzki J., Winniewisser G., 2005, *Journal of Molecular Structure*, 742, 215
- Pavlenko Y. V., Yurchenko S. N., Tennyson J., 2020, *Astronomy & Astrophysics*, 633
- Polyansky O. L., Kyuberis A. A., Lodi L., Tennyson J., Yurchenko S. N., Ovsyannikov R. I., Zobov N. F., 2017, *Monthly Notices of the Royal Astronomical Society*, 466, 1363
- Qin Z., Bai T., Liu L., 2021, *Journal of Quantitative Spectroscopy and Radiative Transfer*, 258, 107352
- Rey M., Nikitin A. V., Babikov Y. L., Tyuterev V. G., 2016, *Journal of Molecular Spectroscopy*, 327, 138
- Riechers D. A., Walter F., Cox P., Carilli C. L., Weiss A., Bertoldi F., Neri R., 2007, *The Astrophysical Journal*, 666, 778
- Riffel R., Pastoriza M. G., Rodríguez-Ardila A., Maraston C., 2007, *The Astrophysical Journal*, 659, L103
- Ritchey A., Federman S., Lambert D. L., 2011a, *The Astrophysical Journal*, 728, 36
- Ritchey A. M., Federman S. R., Lambert D. L., 2011b, *Astrophysical Journal*, 728, 36
- Sauval A. J., Tatum J. B., 1984, *The Astrophysical Journal Supplement Series*, 56, 193
- Shi D., Li W., Sun J., Zhu Z., 2011, *Journal of Quantitative Spectroscopy and Radiative Transfer*, 112, 2335
- Shinnaka Y., et al., 2017, *The Astronomical Journal*, 154, 45
- Skatrud D. D., De Lucia F. C., Blake G. A., Sastry K., 1983, *Journal of Molecular Spectroscopy*, 99, 35
- Snedden C., Lucatello S., Ram R. S., Brooke J. S. A., Bernath P. F., 2014, *The Astrophysical Journal Supplement Series*, 214, 26
- Syme A.-M., McKemmish L. K., 2020a, *Research Notes of the AAS*, 4, 139
- Syme A.-M., McKemmish L. K., 2020b, *Monthly Notices of the Royal Astronomical Society*, 39, 25
- Syme A.-M., Mousley A., Cunningham M., McKemmish L. K., 2019, *Australian Journal of Chemistry*, 73, 743
- Tautvaišienė G., et al., 2020, *The Astrophysical Journal Supplement Series*, 248, 19
- Tennyson J., Yurchenko S. N., 2017, *International Journal of Quantum Chemistry*, 117, 92
- Tennyson J., et al., 2016, *Journal of Molecular Spectroscopy*, 327, 73
- Tennyson J., et al., 2020, *Journal of Quantitative Spectroscopy and Radiative Transfer*, 255
- Thomson R., Dalby F. W., 1968, *Canadian Journal of Physics*, 46, 2815
- Wagner R. M., Schleicher D. G., 1997, *Science*, 275, 1918
- Welty D. E., Sonnentrucker P., Snow T. P., York D. G., 2020, *The Astrophysical Journal*, 897, 1
- Western C. M., 2017, *Journal of Quantitative Spectroscopy and Radiative Transfer*, 186, 221
- Yin Y., Shi D., Sun J., Zhu Z., 2018, *The Astrophysical Journal Supplement Series*, 235, 120
- Yurchenko S. N., Lodi L., Tennyson J., Stolyarov A. V., 2016, *Computer Physics Communications*, 202, 262
- Yurchenko S. N., Al-Refaie A. F., Tennyson J., 2018, *Astronomy and Astrophysics*, 614, 131
- Yurchenko S. N., Lodi L., Tennyson J., Stolyarov A. V., 2020, Duo: a general program for the calculation of spectra of diatomic molecule. User's manual. <https://github.com/Trovemaster/Duo/tree/master/manual>